

Influence of native defects on magneto-optoelectronic properties of α -MoO₃

Poonam Sharma,^{1,*} Vikash Mishra,^{1,†} and Alok Shukla^{1,‡}

¹*Department of Physics, Indian Institute of Technology Bombay, Mumbai 400076, India*

Semiconducting oxides possess a variety of intriguing electronic, optical, and magnetic properties, and native defects play a crucial role in these systems. In this study, we study the influence of native defects on these properties of α -MoO₃ using the first-principles density functional theory (DFT) calculations. From the formation energy calculations, it is concluded that Mo vacancies are difficult to form in the system, while O and Mo-O co-vacancies are energetically quite favorable. We further find that vacancies give rise to mid-gap states (trap states) that remarkably affect the magneto-optoelectronic properties of the material. Our calculations indicate that a single Mo vacancy leads to half-metallic behavior, and also induces a large magnetic moment of 5.98 μ_B . On the other hand, for the single O vacancy case, the band gap disappears completely, but the system remains in a non-magnetic state. For Mo-O co-vacancies of two types considered in this work, a reduced band gap is found, along with an induced magnetic moment of 2.0 μ_B . Furthermore, a few finite peaks below the main band edge are observed in the absorption spectra of configurations with Mo and O vacancies, while they are absent in the Mo-O co-vacancies of both types, just like in the pristine state. From the ab-initio molecular dynamics simulations, stability and sustainability of induced magnetic moment at room temperature is verified. Our findings will enable the development of defect strategies that maximize the functionality of the system, and further help in designing highly efficient magneto-optoelectronic and spintronic devices.

I. INTRODUCTION

In recent years, transition metal oxides have been intensely investigated by the research community due to their extensive usage in various fields such as field emission devices [1], storage devices [2–4], light-emitting diodes [5–7], high-power transistors, and other optoelectronic devices. In particular, molybdenum trioxide (MoO₃), which is an n-type semiconductor, is a well-known transition metal oxide owing to its high dielectric constant, high work function (i.e., ~ 6.8 eV), and tunable semiconducting characteristics [6, 8, 9]. The layers of this material are easily peeled away from the bulk crystal because of the weak van der Waals (vdW) interaction between them. Moreover, due to having effective hole transport in α -MoO₃, it is a good candidate for use in photodetectors [10], field-effect transistors [11], field-effect biosensors [12], gas sensors [13], resistive memory devices [14], electrochromic and photochromic devices [3], and supercapacitor applications [15]. It has been observed that MoO₃ typically crystallizes in three phases, namely α -MoO₃ (orthorhombic structure), β -MoO₃ (monoclinic structure), and hexagonal MoO₃. Octahedron composed of MoO₆ provides a primary framework for synthesizing different phases of MoO₃. Double layers of octahedral MoO₆ connect with van der Waals (vdW) interaction to form the layered orthorhombic phase of α -MoO₃. In the past, α -MoO₃ has been synthesized using various experimental techniques [16–21], and studies reveal that α -MoO₃ with the orthorhombic structure is the most stable phase.

Measurements show that the experimental band gap of α -MoO₃ lies in the range of 3.0–3.3 eV [22–24]. Huang *et al.* performed the density functional theory (DFT) calculations, including vdW interactions, and obtained an indirect band gap of 1.62 eV [25]. Li *et al.* performed PBE+D2 calculations for the single-layer and bulk phase of MoO₃ and predicted an indirect band gap of 1.73 eV and 1.71 eV, respectively [26]. Akande *et al.* performed the GGA+U calculation by considering two different U values. By applying U = 4.3 and 6.3 eV on Mo(*d*) orbitals, they observed a good agreement of lattice constants with experimental values, but the band gap was found to be close to 2 eV for both values of U [27]. Inzani *et al.* investigated the influence of van der Waals dispersion effects, and also included several U corrections on Mo(*d*) orbitals [28]. They concluded that, while the dispersion correction improves the description of the crystal structure significantly, a change in U value applied on Mo (*d*) orbitals from 2 to 8 eV has essentially no influence on the band gap. Das *et al.* also studied the properties of MoO₃ at the DFT+U/D₃ and DFT+U/D₃/SO levels [29] of theory by applying U = 5 eV on Mo(*d*) orbitals, and observed a decrement in the band gap to 1.65 eV, as compared to PBE value of 1.99 eV. Interestingly, the authors also applied U corrections on the delocalized O 2*p* orbitals and obtained much-improved results on the properties such as the indirect band gap of the system, lattice parameters, formation enthalpy, static dielectric constant, and dissociation energy of O₂ were computed accurately. The authors concluded that applying U correction in the range 3 to 7 eV on Mo(*d*) orbitals results in worsening of the band gap values and recommended a U correction only on O 2*p* orbitals while studying other properties of bulk MoO₃. In all the studies discussed above, the computed band gap is well below the experimental value. However, Peelaers *et al.* [30] performed

* pspoonamsharma44@gmail.com

† vikash2035@gmail.com

‡ shukla@iitb.ac.in

hybrid functional (HSE06) based calculations to match the band gap value with the experimental data. Their research shows an indirect band gap of 3.19 eV. Qu *et al.* reported a band gap of 2.884 eV [31], and Akande *et al.* reported a band gap of 3.1 eV [27] using the HSE06 functional.

Additionally, a lot of work has been done to narrow the band gap of α -MoO₃ in order to exploit it for solar energy applications [32]. In the pure polycrystalline material, it is well established that there will be a significant number of defects and impurities in the system [33, 34]. Even the presence of a small number of defects in the crystal geometry influences the magneto-optoelectronic properties of the material in a non-trivial manner, as a result, many researchers have focused on understanding the performance of devices in the presence of lattice imperfections. The behavior of defects largely depends on the nature of the material. For example, in oxide materials such as MgO, the excess number of electrons introduced into the system due to oxygen defects are localized on its surface, whereas in the case of TiO₂, electrons are delocalized [35]. Photoluminescence spectroscopy [36], Raman spectroscopy [37], valence band spectroscopy [35], and first-principle calculations studies [38–40] have been widely used to probe the signature of defects in oxide systems. Defects introduce some additional states (trap states) in the band gap region (between the valence and conduction band) that drastically change the magneto-optoelectronic properties of the system. For better device performance and other applications, there is obviously a need to understand not just the origin of defects, but also their influence on other properties. Many researchers have employed the first-principles DFT-based calculations for this purpose and computed not just the magneto-optoelectronic properties in the presence of defects, but also the stability of the native defects in semiconducting oxides [41].

Theoretically and experimentally, previously vacancy-induced magnetism studies in oxide materials, such as ZnO, Y₂O₃, TiO₂, SnO₂, HfO₂, etc., have been extensively performed [42–49]. For example, Elfimov *et al.* performed DFT calculations on CaO and found that a single Ca vacancy induced a magnetic moment of $2 \mu_B$ at 3.125 at% of vacancy concentration, 88% contribution to the magnetic moment comes from the O ions, i.e., nearest neighbors of Ca vacancy, and the system becomes half-metallic ferromagnetic [46]. In the O vacancy, the system still shows non-magnetic behavior. Pemmaraju *et al.* performed the DFT study on HfO₂ by considering a $2 \times 2 \times 2$ supercell having 96 atoms and reported that a single Hf vacancy (i.e., 3.125 at%) induced a magnetic moment of $3.5 \mu_B$, while O vacancy (i.e., 1.562 at%) does not induce any magnetic moment in the system [45]. Khalid *et al.* reported from Positron annihilation spectroscopy measurements and further confirmed by DFT calculations that Zn vacancies are responsible for inducing magnetism in ZnO [49]. Rahman *et al.* studied the defects-induced magnetism in SnO₂ and Li-doped

SnO₂ [47, 48]. In defects induced magnetism study of SnO₂, the authors reported that a single Sn vacancy at the vacancy concentration of 6.25 at% induced a magnetic moment of $4.0 \mu_B$, where O atoms surrounded by the Sn vacancy defect contribute the most to the magnetic moment. In the case of a single O vacancy, the system still remains non-magnetic. Further, Pandey *et al.* studied the impact of Sr, Ti, and O vacancy defects on the electronic and optical properties of TiO₂ and SrTiO₃ [50]. From the experimental measurements, the authors found that vacancy defects enhance optoelectronic properties, such as photocurrent, optical absorption, etc. Wang *et al.* studied the effect of O vacancy defects on the electronic and optical properties through Raman spectroscopy, photoluminescence spectroscopy, absorption spectroscopy, and photoemission spectroscopy in the V₂O₅ nanowires [51]. Due to O vacancy defects, an increase in the optical band gap from 1.95 eV to 2.45 eV was found. We believe that similar to these works on other transition metal oxides, a study of the magnetic and optical properties of defective α -MoO₃ is also worthwhile.

Therefore, in this work, we undertake a systematic study of the variation of magneto-optoelectronic properties of α -MoO₃ with different defects (vacancies) and also to understand the stability of the system in response to these defects. In most previous studies of vacancies in α -MoO₃, predominantly O vacancies were considered [28, 30, 52, 53]. In the present work, along with the O vacancy, the Mo vacancy, and Mo-O co-vacancies have also been considered. A systematic study using first-principles DFT calculations on pristine and self-deficient α -MoO₃ has been carried out, and the obtained results are compared with existing experimental and theoretical results.

II. COMPUTATIONAL DETAILS

Spin-polarized DFT calculations were carried out using the Vienna Ab-initio Simulation Package (VASP) code [54, 55] in conjunction with the projector augmented wave (PAW) pseudopotentials method [56, 57]. The generalized gradient approximation (GGA), as implemented in the Perdew-Burke-Ernzerhof (PBE) functional, was employed in the calculations [58]. In order to benchmark our GGA results, we also repeated some of our calculations using HSE06 functional [31]. Convergence tests were carried out systematically for the plane-wave cutoff energy and for the number of k-point used in the sampling of the Brillouin Zone (BZ). A plane-wave basis set with an energy cutoff of 500 eV has been used throughout the calculations. For BZ sampling, Monkhorst-pack [59] mesh with a k-point grid $5 \times 10 \times 9$ was used for geometry optimization of the unit cell, and $7 \times 12 \times 11$ for the density of states calculations. The unit cell of α -MoO₃ contains 16 atoms. The valence electronic configurations of Mo and O atoms for the PAW pseudopotentials were taken

as $4p^65s^14d^5$, and $2s^22p^4$, respectively. We optimized the atomic coordinates along with the lattice parameters of the pristine α - MoO_3 unit cell. The convergence criterion of the Hellman-Feynman force on all atoms was set to 5×10^{-3} eV, while the energy threshold was fixed at 10^{-5} eV. *Ab-initio* molecular dynamics (AIMD) simulations were performed at 300 K to check the stability and sustainability of the defects-induced magnetic moment using canonical ensemble (NVT) for a time period of 5 ps, with the step size of 1 fs.

To study the optical properties of the system, we have computed the complex dielectric function and, subsequently, the absorption coefficients, using Ehrenreich and Cohen's [60] formalism. The frequency (ω) dependent complex dielectric function $\epsilon(\omega)$ is given as

$$\epsilon(\omega) = \epsilon_1(\omega) + i\epsilon_2(\omega), \quad (1)$$

where, $\epsilon_1(\omega)$ and $\epsilon_2(\omega)$ denote the real and imaginary part of the dielectric function, with $\epsilon_2(\omega)$ defined as

$$\epsilon_2(\omega) = \frac{e^2 \hbar}{\pi m^2 \omega^2} \sum_{v,c} \int_{BZ} |u_{c\mathbf{k}}| \hat{\mathbf{e}} \cdot \nabla |u_{v\mathbf{k}}|^2 \delta[\omega_{cv}(\mathbf{k}) - \omega] d^3k. \quad (2)$$

Above, the matrix element $\langle u_{c\mathbf{k}} | \hat{\mathbf{e}} \cdot \nabla | u_{v\mathbf{k}} \rangle$ corresponds to the direct transitions between the valence and the conduction states, $\hat{\mathbf{e}}$ represents the polarization vector of the incident photon, $\omega_{cv}(\mathbf{k}) = E_{c\mathbf{k}} - E_{v\mathbf{k}}$ denotes the excitation energy, and $u_{c\mathbf{k}}$ and $u_{v\mathbf{k}}$ are the periodic Bloch wave functions of wave vector \mathbf{k} for the conduction and valence states, respectively. Moreover, the Kramers-Kronig relations can be used for the calculation of the real part $\epsilon_1(\omega)$ from $\epsilon_2(\omega)$

$$\epsilon_1(\omega) = \frac{2}{\pi} p \int_0^\infty \frac{\omega' \epsilon_2(\omega')}{\omega'^2 - \omega^2} d\omega', \quad (3)$$

where p denotes the principle value of the integral. The two dielectric functions are then used to calculate the reflectivity, absorption coefficient, refractive index, electron energy-loss spectrum, and other constants [61]. In this work, we compute and analyze the absorption coefficient $\alpha(\omega)$ given as

$$\alpha(\omega) = \frac{\sqrt{2}\omega}{c} \left(\sqrt{(\epsilon_1(\omega))^2 + (\epsilon_2(\omega))^2} - \epsilon_1(\omega) \right)^{\frac{1}{2}}. \quad (4)$$

Moreover, it is necessary to know the formation energies when studying the effect of defects or impurities on the electronic structure because they describe the stability of the defective systems. We have used the following equation (Eq. 5) for the calculation of the formation energies of systems with defects

$$E_{form} = E_{defect} - E_{pristine} + \sum_k \Delta n_k u_k + q(E_{VBM} + E_F). \quad (5)$$

Above, E_{defect} is the energy of the defective system, whereas $E_{pristine}$ denotes the energy of the pristine system. Furthermore, Δn_k is the number of k types of atoms

that are removed from the system and u_k is their chemical potential. The exchange of electrons in charged systems with charge q is represented by the formula $q(E_{VBM} + E_F)$, where E_F is the Fermi level, and E_{VBM} shows the valence-band maximum energy in the pristine system.

III. RESULTS AND DISCUSSION

A. Structure Analysis

In this work we study the orthorhombic phase of molybdenum trioxide (α - MoO_3) with the space group symmetry Pnma (62). Lattice parameters of the pristine α - MoO_3 unit cell after performing geometry optimization were found to be $a = 14.80$ Å, $b = 3.72$ Å, $c = 3.97$ Å [27], and in Fig. 1(a) we show the optimized structure for its $2 \times 2 \times 1$ supercell.

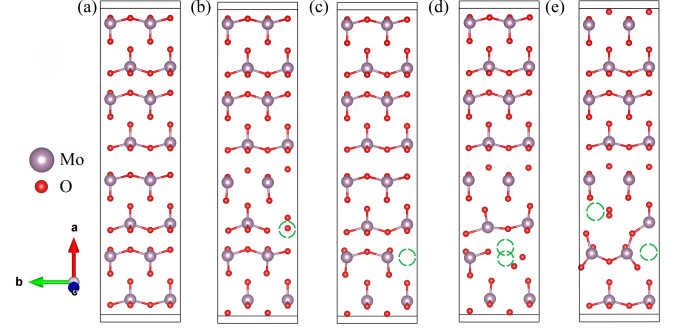


FIG. 1. The optimized $2 \times 2 \times 1$ supercell structures of α - MoO_3 : (a) pristine structure, (b) with a single Mo vacancy, (c) with a single O vacancy, and (d,e) with Mo-O co-vacancies of types P1 and P2, respectively. Small green circles show the vacant positions of the respective atoms.

To study the variation of magneto-opto-electronic properties for various types of defects (different types of vacancies) are created in $2 \times 2 \times 1$ supercell. Figs. 1(b)-1(e) show the optimized $2 \times 2 \times 1$ supercell structure of α - MoO_3 with Mo vacancy (V_{Mo}), O vacancy (V_O), and Mo-O co-vacancies (V_{Mo+O}) of types P1 and P2, respectively.

B. Band Structure and Density of States

1. Pristine Material

Firstly, we studied the ground-state electronic properties of α - MoO_3 using spin-polarized DFT simulations. The total density of states (TDOS) and band structure of pristine α - MoO_3 calculated using the GGA and HSE06 functionals are presented in Figs. 2(a)-2(d). The GGA-level TDOS plot (see Figs. 2(a)) clearly shows symmetry between the up and down spin states indicating non-magnetic behavior, and a finite band gap. As shown in

the PBE band structure plot (Fig. 2(c)), we obtain an indirect band gap of 1.8 eV [31]. Along the high-symmetry directions corresponding to Γ -X and R-T, almost degenerate eigenvalues are obtained in the valence and conduction bands. Furthermore, the valence band maxima (VBM) and conduction band minima (CBM) are positioned at T and Γ points, respectively. Our results on the band structure are in good agreement with the previously reported results [31, 62]. In addition, we performed GGA+U calculations to match our band gap with the experimental value. We first applied U correction in the range 2 to 12 eV, only on Mo(4d) electrons. However, the maximum value of the calculated band gap was 2.54 eV for $U=9.0$ eV, which is still not in good agreement with the experimental value of 3.0-3.3 eV [22–24]. Given the fact that PDOS (see Fig. 3) analysis reveals that the VBM is entirely composed of O 2p orbitals, thus, next we applied the U correction also to the O(2p) electrons, in addition to Mo(4d) ones. We found that the choice $U(2p) = 7$ eV for O and $8 \leq U(4d) \leq 12$ eV for Mo does improve the band gap in the sense that it is closer to the experimental value. However, the calculations predict the band gap of the minority spin to be significantly larger than that of the majority spin. Similar behavior is also found in the case i.e., $U > 9$ eV on Mo(4d) electrons. This result is in complete contradiction with our GGA and HSE06 results, therefore, we conclude that the DFT+U approach is yielding erroneous results for this system. Therefore, we repeated our calculations using a more accurate hybrid functional, i.e., HSE06, and the results are presented in Figs. 2(b) and 2(d). Indeed, we found an indirect band gap of 2.99 eV using the HSE06 functional, which is in excellent agreement with the experimental value [19]. But, we note that the band structure computed using the HSE06 functional is quite similar to that obtained from GGA, except for the increased band gap.

Further, to achieve a better understanding of the contribution of different orbitals in the TDOS, we have calculated the projected density of states (PDOS) of Mo and O atoms, and presented it in Figs. 3(a) and 3(b), respectively. We have computed the PDOS for the 5s and 4d orbitals of the Mo atom, along with the 2s and 2p orbitals of the O atom. From the figure, it is obvious that the majority of the contribution to the TDOS comes from the 4d orbitals of Mo and 2p orbitals of the O atom. Furthermore, the dominant contribution to the TDOS near the Fermi energy is obtained from the 2p orbital of the O atom.

2. Defective Material

Next, we studied the vacancy-induced electronic properties of α -MoO₃, and for this purpose, we first created Mo, O, and Mo-O co-vacancies of types P1 and P2 in the $2 \times 2 \times 1$ supercell, followed by geometry optimization. From the optimized geometry in each case, the band

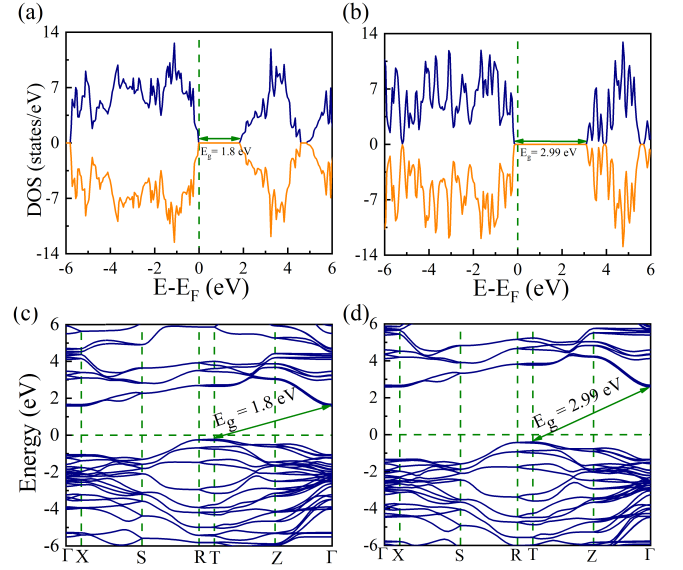


FIG. 2. (a,b) The total density of states and (c,d) electronic band structure of pristine unit cell of α -MoO₃ using PBE and HSE06 functional, respectively.

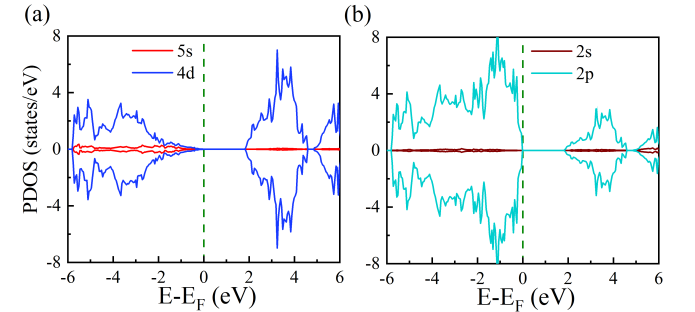


FIG. 3. Partial density of states of (a) Mo (5s and 4d orbitals) and (b) O (2s and 2p orbitals) atoms using GGA.

structure, DOS, and optical absorption spectrum were computed. We computed the optical absorption spectra because, experimentally, defect signatures are successfully investigated in oxide samples using optical absorption spectroscopy [33, 34, 63]. Furthermore, DOS can be used for interpreting the experiments, which are performed using transmission electron microscopy [64] and scanning tunneling microscopy [65], thus revealing information on such intrinsic defects in the system. In bulk systems, defect states become very sensitive to the variation in the position of defects in the supercell. The purpose of considering two types of co-vacancies in the supercell is to see whether, or not, the magneto-optoelectronic properties change in the oxides samples with the relative locations of the vacancies.

In Figs. 4(a)-4(d), we present the TDOS corresponding to the cases with Mo, O, and Mo-O co-vacancies of types P1 and P2, respectively, using GGA. It is obvious from the figures that the electronic properties of the

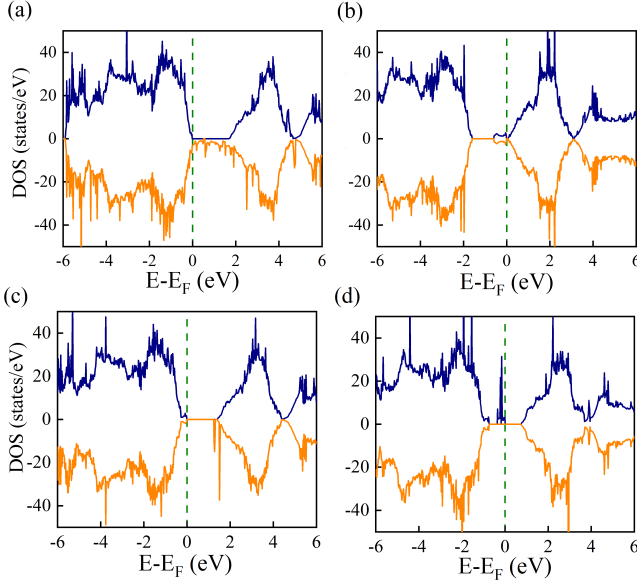


FIG. 4. The total density states of α - MoO_3 ($2 \times 2 \times 1$ supercell) with (a) Mo vacancy, (b) O vacancy, and Mo-O co-vacancies of types (c) P1 and (d) P2, respectively, using GGA.

material change significantly after the introduction of vacancies leading to the appearance of the mid-gap states. With a Mo vacancy (see Fig. 4(a)) that corresponds to 6.25 at% of vacancy concentration, the system becomes half-metallic with a band gap of 1.63 eV in the majority spin states, while minority spin states show metallic behavior. For the case of O vacancy (see Fig. 4(b)) that corresponds to 2.08 at% of vacancy concentration, the band gap disappears completely due to the emergence of mid-gap states. Previously, Noby *et al.* experimentally showed the impact of O vacancy on α - MoO_3 by considering different oxidizing (oxygen gain) and reducing (oxygen loss) atmospheres [66]. They prepared the samples in different atmospheres (i.e., as prepared, O_2 -treated, H_2 -treated, N_2 -treated and vacuum-treated) and found that the increase in the O vacancies/deficiency led to an increase in electrical conductivity, i.e., a transition from the semi-insulating to the conducting behavior. Chiam *et al.* investigated the defects-stability in α - MoO_3 and its role in organic solar cells [67]. They also investigated the presence of mixed oxidation states of Mo (i.e., 4^+ , 5^+ and 6^+); as a result of this, they concluded that the defects/vacancies play an important role in the enhancement of device performance. In the case of both types of Mo-O co-vacancies, different band gaps are obtained. A reduced band gap is found in both the P1 and P2 co-vacancies. With the P1 (P2) type of co-vacancy, a band gap of 1.39 (0.78) eV is computed due to the majority spin-states, while minority spin-states show a band gap of 1.23 (1.47) eV. Further, Figs. 5(a)- 5(h) show the band structure for the spin-up and spin-down states corresponding to single Mo, O, and Mo-O co-vacancies of P1 and P2 types in the $2 \times 2 \times 1$ supercell, respectively. For O

vacancy (see Figs. 5(c) and 5(d)), the band structure is identical for the spin-up and spin-down states, which signifies that the system remains non-magnetic in the case of O vacancy. For the Mo vacancy (see Fig. 5(a) and 5(b)), a magnetic moment of $5.98 \mu_B$ is obtained, while in the case of Mo-O co-vacancies (see Fig. 5(e)- 5(h) irrespective of their types (i.e., P1 and P2), a magnetic moment of $2.0 \mu_B$ is computed. Here, we also highlight the fact that our obtained results are valid for the Mo vacancy concentration of 6.25 at% and an O vacancy concentration of 2.08 at%. However, in dilute defect limits, the vacancy-induced states, in all likelihood, will be much more localized, as a result of which a single vacancy may not be able to change the transport behaviour of samples from semiconducting to half-metallic/metallic. In Fig. 6, through a schematic, we demonstrate the formation of an O-vacancy-induced mid-gap state between the VBM and CBM, which is nothing but a trap state. The trap states have additional electrons that modify the magneto-optoelectronic properties of the defective system, as compared to the pristine one. In order to achieve a deeper understanding of the nature of mid-gap states, we computed the PDOS, and our results are presented in Fig. 7. It is clear from the PDOS plot that for the case of Mo vacancy (Fig. 7(a) and Mo-O co-vacancies of both types ((Figs. 7(c) and 7(d)), the contribution to the defect states is more from the O atoms, while for the case of O vacancy (Fig. 7(b), Mo atoms contribute remarkably to the defect states.

Next, we repeated our defect calculations with the hybrid functional, i.e., HSE06, in order to verify our GGA-based results. In the MO-vacancy case (see Fig. 8(a)), our HSE06 calculations reveal the half-metallic nature of the system, as obtained in our GGA results as well. While minority spin states exhibit metallic behavior, the band gap in the majority spin states is computed to be 2.33 eV, which is higher than the GGA computed band gap of 1.63 eV. Moreover, a magnetic moment of $6.0 \mu_B$ is obtained that matches well with our GGA computed magnetic moment of $5.98 \mu_B$. In the O vacancy case (see Fig. 8(b)), HSE06 functional predicts the system to be metallic in agreement with our GGA results. Further, the system continues to be non-magnetic; up-spin and down-spin states show symmetrical nature, supporting our GGA findings (see Fig. 4(b)). In P1 and P2 co-vacancies (see Fig. 8(c-d)), semiconducting nature is reported for both, with band gaps of 2.45 eV and 2.66 eV, respectively, which are significantly larger than the corresponding gaps obtained in the GGA calculations. A magnetic moment of $2 \mu_B$ is obtained in both types of co-vacancies in HSE06 calculations, in full agreement with the GGA results.

C. Spin density analysis

We performed the spin density analysis to understand the contribution of Mo and O atoms to the magnetic

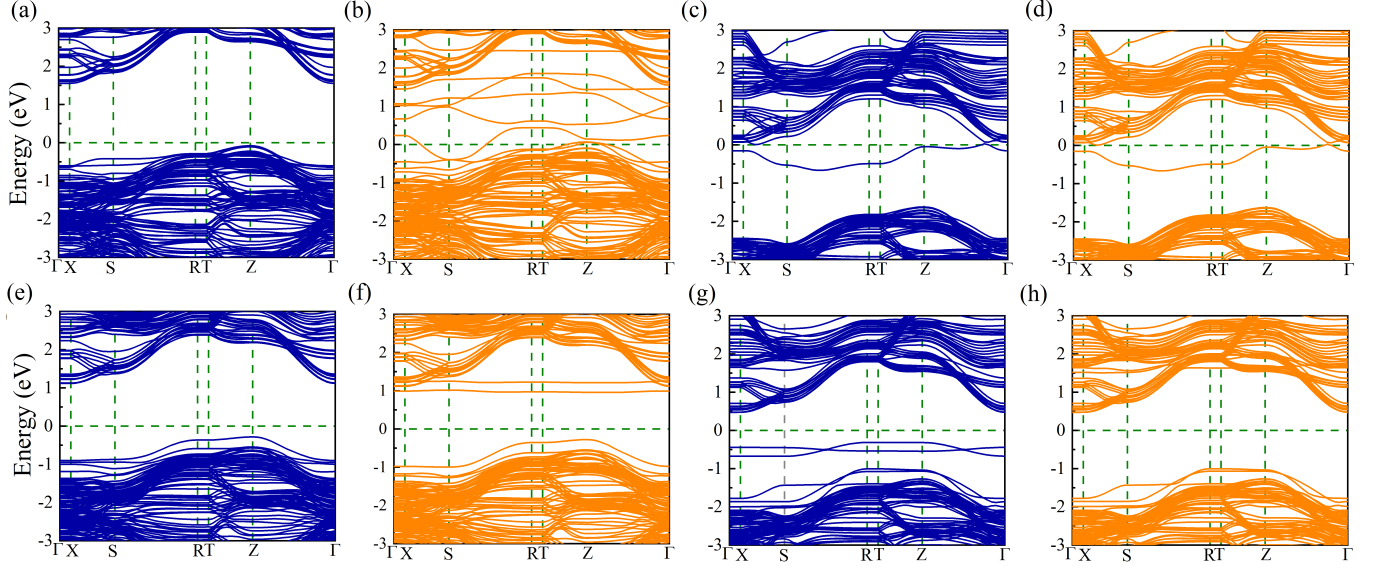


FIG. 5. Electronic band structure of α - MoO_3 ($2 \times 2 \times 1$ supercell) with (a,b) Mo vacancy, (c,d) O vacancy, and Mo-O co-vacancies of types (e,f) P1 and (g,h) P2 for the spin-up and spin-down states, respectively.

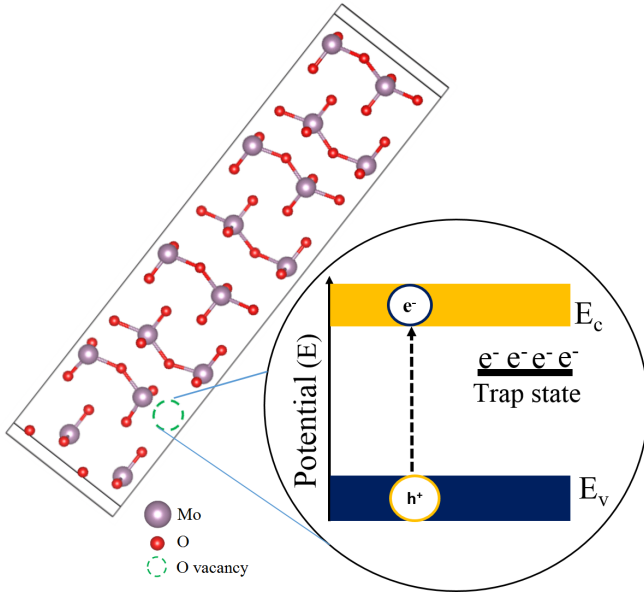


FIG. 6. Schematic diagram showing the formation of a vacancy-induced trap state in between the valence band maxima (VBM) and conduction band minima (CBM).

moment induced in different vacancy configurations of $2 \times 2 \times 1$ supercell of α - MoO_3 . Figs. 9(a)- 9(c) show the spin density plots obtained by subtracting the up-spin (ρ_{\uparrow}) and down-spin (ρ_{\downarrow}) channels of charge densities correspond to the Mo vacancy and Mo-O co-vacancies of types P1 and P2, for the isovalues of 0.099e, 0.007e, and 0.041e, respectively. As shown in the figures, the spin density isosurface (shown in yellow color) is mostly concentrated around the O atoms (nearest neighbor atoms of

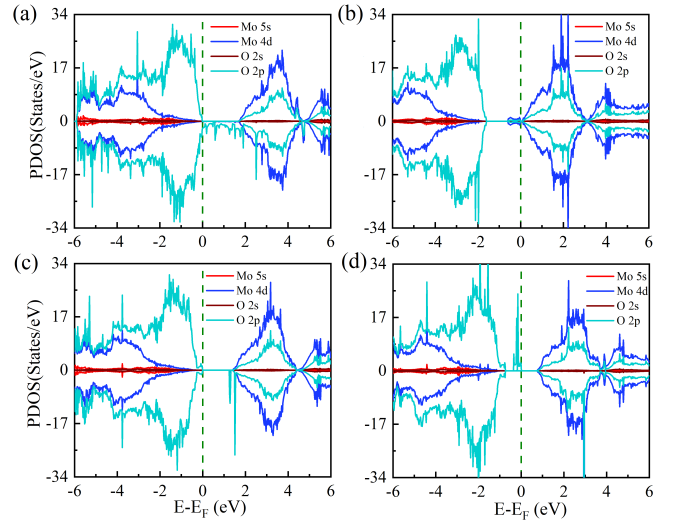


FIG. 7. Partial density of states (PDOS) of Mo (5s and 4d orbitals) and O (2s and 2p orbitals) in α - MoO_3 $2 \times 2 \times 1$ supercell computed using the GGA with (a) Mo vacancy, (b) O vacancy, and for (c,d) Mo-O co-vacancies of types P1 and P2, respectively.

vacancies) in all three cases, which reflects the fact that in all three cases, the contribution from O atoms is more to the magnetic moment. Our spin density plots are qualitatively compatible with the PDOS analysis (see Fig. 7). In addition, the spin density isosurface is dumbbell-shaped, indicating a higher contribution of the p orbitals of oxygen to the induced magnetic moments.

D. Practical feasibility

We computed the formation energy for (i) Mo vacancy, (ii) O vacancy, and (iii) Mo-O co-vacancies of both types, i.e., P1 and P2, respectively, for the practical realization of the systems with respect to these defect configurations. Before discussing the formation energy of different defect configurations, first, we calculated the formation energy for pristine α -MoO₃ by considering metallic Mo and O₂ gas using the formula

$$\begin{aligned} E_{form}^{MoO_3} &= \mu_{Mo}^{MoO_3} + 3\mu_O^{MoO_3} - (\mu_{Mo}^0 + 3\mu_O^0) \\ &= E_{MoO_3} - (\mu_{Mo}^0 + 3\mu_O^0). \end{aligned} \quad (6)$$

Where E_{MoO_3} is the total energy of the pristine α -MoO₃ energy per formula unit, and $\mu_{Mo}^{MoO_3}$ and $\mu_O^{MoO_3}$ are the chemical potentials of Mo and O in α -MoO₃. Moreover, μ_{Mo}^0 and μ_O^0 are the chemical potential of Mo and O in pure molybdenum metal and O₂ gas, respectively.

Using Eq. 6, and the obtained values in our DFT simulations, i.e., $E_{MoO_3} = -32.88$ eV, $\mu_{Mo}^0 = -10.94$ eV, and $\mu_O^0 = 0.5 \times (-9.77) = -4.885$ eV, we calculated $E_{form}^{MoO_3} = -7.27$ eV, which is in good agreement with the theoretically reported value of -6.77 eV [29] and the experimental value of -7.72 eV [68]. A good matching of formation energy with the previously reported theoretical and experimental results gives us confidence and shows the correctness of our simulation methods.

Next, we calculated the formation energy for the defective systems using Eq. 5, as discussed previously. Using the stability conditions, the following range of chemical potentials for Mo and O have been derived and further used in the formation energy calculation of the defective

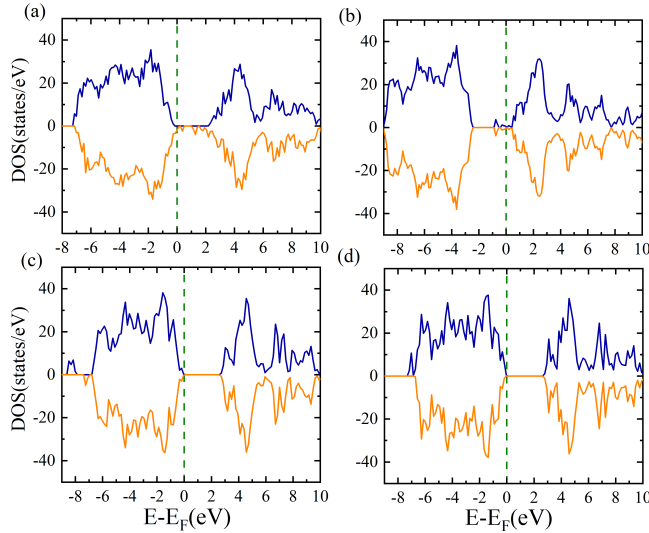


FIG. 8. The total density states of α -MoO₃ ($2 \times 2 \times 1$ supercell) with (a) Mo vacancy, (b) O vacancy, and Mo-O co-vacancies of types (c) P1 and (d) P2, respectively, using HSE06.

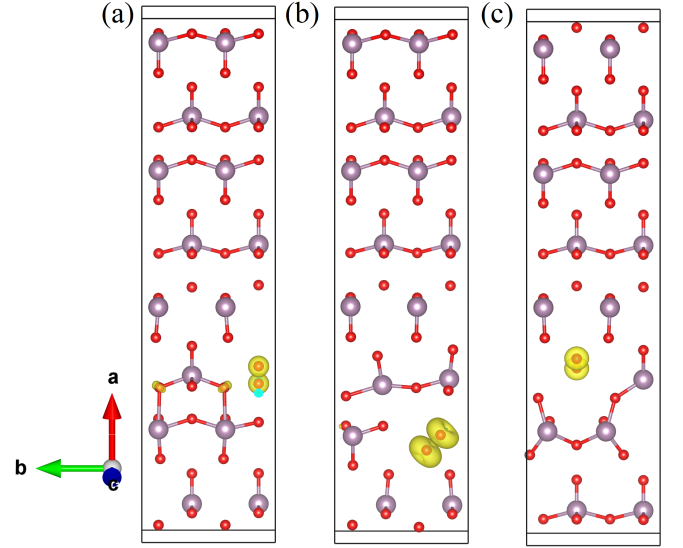


FIG. 9. The spin density plots ($\Delta\rho = \rho_{\uparrow} - \rho_{\downarrow}$) of $2 \times 2 \times 1$ supercell of α -MoO₃ using GGA with the (a) Mo vacancy for the isovalue of 0.099e and (b,c) Mo-O co-vacancies of types P1 and P2 for the isovalue of 0.007e and 0.041e, respectively.

system

$$\mu_{Mo}^{min} = \mu_{Mo}^0 + E_{form}^{MoO_3} < \mu_{Mo}^{MoO_3} < \mu_{Mo}^0. \quad (7)$$

$$\mu_O^{min} = \mu_O^0 + \frac{1}{3}E_{form}^{MoO_3} < \mu_O^{MoO_3} < \mu_O^0. \quad (8)$$

In the above equations, μ_{Mo}^0 and μ_O^{min} denote the chemical potentials of Mo and O, in Mo-rich conditions, while μ_{Mo}^{min} and μ_O^0 represent those in O-rich conditions. The calculated value of chemical potential in Mo-rich condition for Mo (O) is -10.94 (-7.30) eV, whereas in the O-rich condition it is -18.22 (-4.88) eV. Our computed results of formation energy corresponding to different vacancy configurations are presented in Table I (Fig. 10).

TABLE I. Formation energies (eV) corresponding to different vacancy configurations in α -MoO₃, in both Mo-rich and O-rich environments .

Vacancy types \rightarrow	V_{Mo}	V_O	$V_{Mo+O(P1)}$	$V_{Mo+O(P2)}$
Mo-rich	14.28	1.69	5.58	6.65
O-rich	7.0	4.11	1.02	1.79

It is clear from Fig. 10 and Table I that the formation energy for Mo vacancy is very high compared to other defect configurations for the entire range of O chemical potential indicating that Mo vacancy is difficult to form at ordinary conditions in α -MoO₃ [30]. Further, O vacancy in the proximity of V_{Mo} (i.e., Mo-O co-vacancies) reduces the formation energy of Mo vacancy considerably. Therefore, our first-principles results indicate that

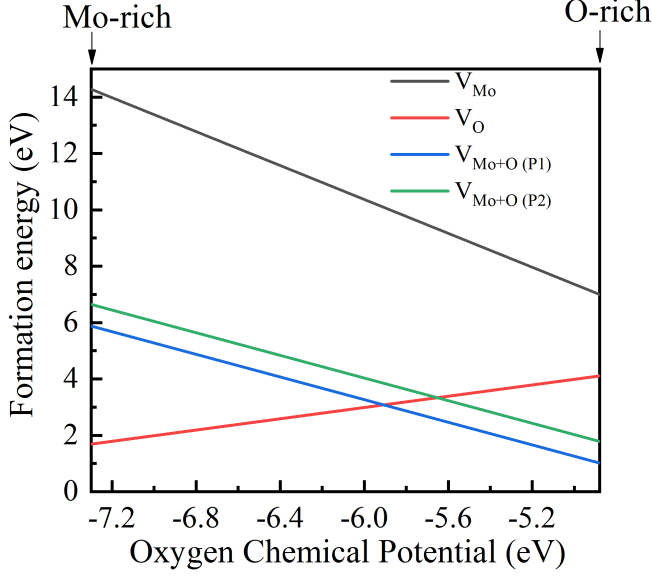


FIG. 10. Formation energy of α - MoO_3 corresponding to different vacancy configurations (as shown in Fig. 1) with respect to O chemical potential. The left side shows the Mo-rich, and the right side shows the O-rich limits.

Mo-O co-vacancies support induced magnetic moment in α - MoO_3 , along with reducing the formation energy, and thus stabilizing the Mo vacancy that is responsible for inducing the magnetic moment in the system, as discussed in the previous section. Further, in the Mo-rich condition (i.e., O-poor), O vacancy has the lowest formation energy of 1.69 eV. Further, for the sake of comparison, we note that Cao *et al.* reported ~ 1.4 eV of formation energy for S vacancy in MoS_2 under Mo-rich condition [69], while Kuklin *et al.* reported 1.64 eV for Se vacancy in PdSe_2 under Pd-rich conditions [70]. Our computed value of formation energy for O vacancy is within the usual range of formation energies reported for transition-metal dichalcogenide systems in the literature. With the increase in O chemical potential, i.e., towards the O-rich limit, Mo-O co-vacancies of both types start dominating and are more stable compared to the O vacancy. Moreover, the P2 type of Mo-O co-vacancy shows 0.77 eV higher formation energy than P1, implying that the P1 type of co-vacancy is more stable, but on the other hand, both types of co-vacancies exhibit lower formation energy than O vacancy. Here we would like to emphasize the fact that experimentally the stoichiometry of the growth circumstances plays a very crucial role and may affect formation energy values significantly [71].

Till now, we discussed the formation energy of neutral vacancies. Next, we considered different charged defect states. We considered +1, +2, -1 and -2 charge states for both Mo and O vacancies and corresponding formation energies are shown in Fig. 11. From the formation energy graphs, it is clear that, as in neutral states, the formation energy of Mo vacancy in different charged states is

still high compared with O vacancy. Further, in the O-vacancy case, in both rich and poor conditions, the +1 and +2 states are more stable compared to the negatively charged states, as reported previously [30]. This clearly indicates that the O-vacancy donates electrons to the conduction band to form a stable state. Therefore, O vacancy behaves like a shallow donor, as shown by Noby *et al.* [66] and is responsible for the unintentional n-type semiconducting behavior of α - MoO_3 .

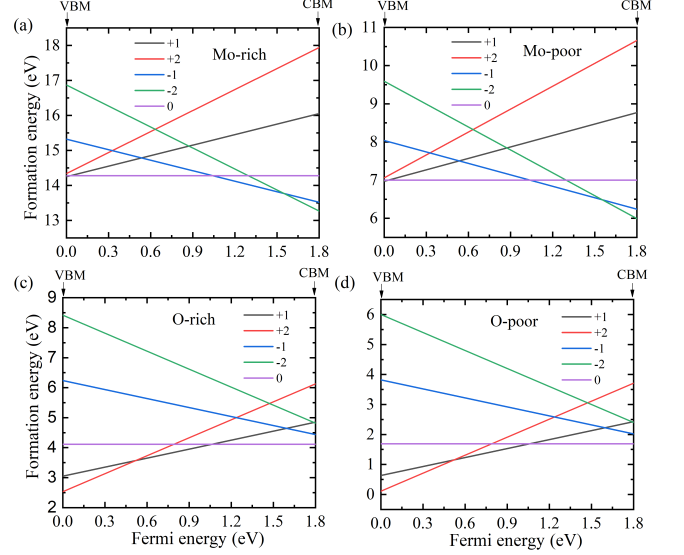


FIG. 11. Charged defects formation energies for the (a,b) Mo vacancy and (c,d) O vacancy in Mo-rich/poor and O-rich/poor conditions as a function of the Fermi energy.

E. Ab-initio MD simulations

In this section, we discuss the results obtained from Ab-initio molecular dynamics (AIMD) simulations, which are performed to investigate the stability and sustainability of the induced magnetic moment, and also to verify the stability of the structure, at room temperature. For technological applications, such as for implementation in spintronic devices, it is important to check not only the structural stability, but also the survival of induced magnetic moments at room temperature. In our study, O vacancy does not induce any kind of magnetic moment in the system, therefore, we performed the AIMD simulations for Mo-O co-vacancy of type P1 owing to the fact that although both types of co-vacancies induce the same magnetic moment (i.e., $2 \mu_B$), the P1 type of co-vacancy is found to be more stable, as discussed earlier.

Experimentally, to favor the P1 type of Mo-O co-vacancy, one can tune the O chemical potential (μ_O) within the stability limits as described in Eq. 8 by using the equation

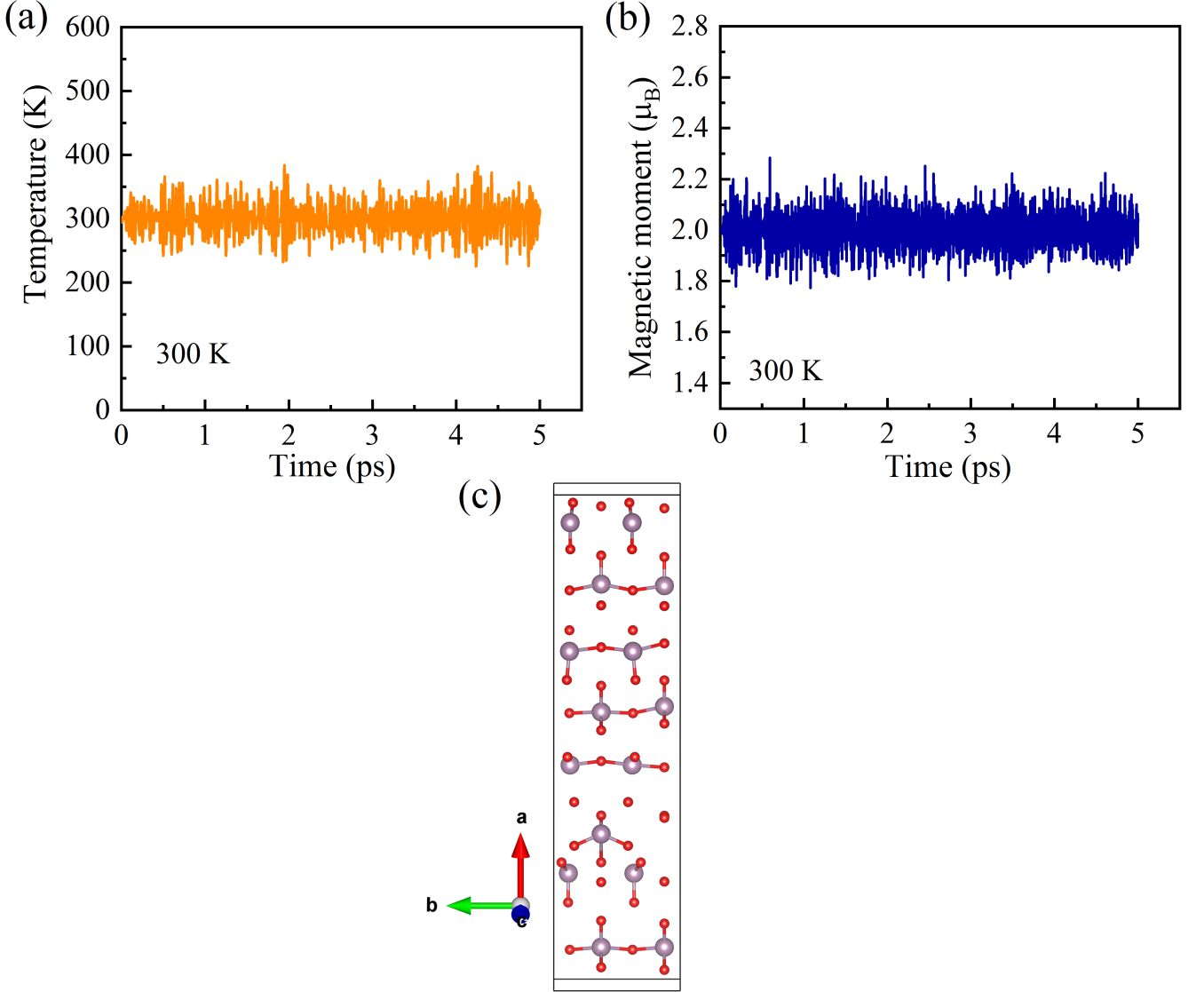


FIG. 12. Variation of (a) temperature and (b) magnetic moment as a function of AIMD simulation steps at the initial temperature 300 K. (c) Mo-O co-vacancy structure of type P1 obtained at 300 K.

$$\mu_O(T, P) = \mu_O(T, P^0) + \frac{1}{2}KT \ln\left(\frac{P}{P^0}\right). \quad (9)$$

Here, T and P denote the temperature and pressure of O₂, K denotes Boltzmann's constant, and $P^0 = 1$ atm.

We performed the AIMD simulations for the time period of 5 ps, with the initial temperature fixed at the room temperature taken to be 300 K. Figs. 12(a) and 12(b) show the variation of temperature and magnetic moment as a function of time. In Fig. 12(c), we show the Mo-O co-vacancy structure of P1 type obtained at 300 K. After a time period of 5 ps, we found that the structure remains stable (Fig. 12(c)) with an average magnetic moment of 2 μ_B , which exactly matches the obtained value of magnetic moment in our DFT results. The induced

magnetic moment is found to be very stable, with minimal variations around 2 μ_B , and sustained at the room temperature (Fig. 12(a)- 12(b)).

F. Optical Absorption Spectra

Now, we analyze the optical properties of the system because the optical characteristics of semiconductor oxide materials have generated tremendous research interest due to their potential use in solar cells, photovoltaic materials, *etc.* In Fig. 13, we present the optical absorption spectra of pristine α -MoO₃ using the GGA approach. Huang *et al.* performed a comprehensive first-principles DFT study of the electronic structure and optical properties of pristine and H-doped α -MoO₃ using

the optB88 functional, and reported an optical gap ≈ 2.0 eV [25]. Experimentally, Itoh *et al.* measured the optical gap of the single crystal α -MoO₃ to be 3.5 eV [72], while in the thin film samples, the corresponding value was found to be 3.1 eV [24, 73, 74]. In our study, we used the convention of Itoh *et al.* for the a and c axes while plotting the optical absorption spectra [72].

From Fig. 13 it is obvious that the optical gaps (the energy marking the onset of optical absorption) obtained in our PBE functional-based calculations for E||a (E||c) are 2.93 (2.60) eV, which are 0.17 (0.5) eV lower than the thin-film values, and 0.57 (0.9) eV below the single-crystal values. Our DFT computed absorption spectra show considerable anisotropic behavior with respect to the polarization (i.e., E||a vs. E||c), as reported previously in single crystal and thin film-based experiments [24, 72–74]. Moreover, in E||a component

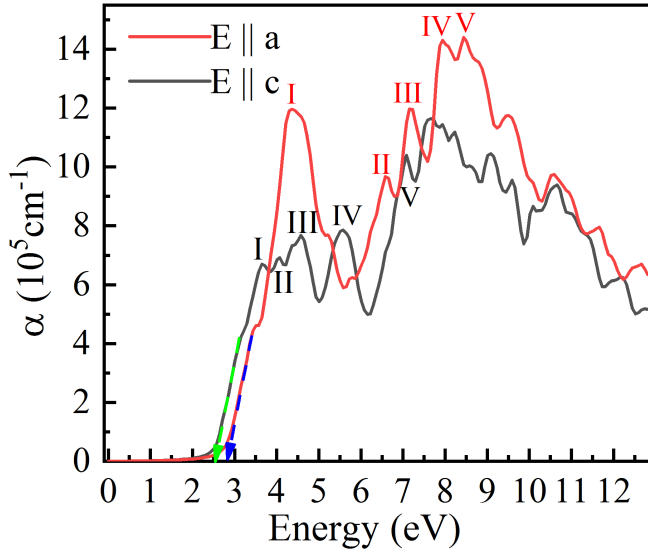


FIG. 13. Our calculated absorption spectra of $2 \times 2 \times 1$ supercell of pristine α -MoO₃ for E||a (red color) and E||c (black color) using the first-principles DFT, employing PBE functional.

of the spectrum, we obtained five different peaks at 4.36 eV, 6.58 eV, 7.22 eV, 7.94 eV, and 8.44 eV. On the other hand, in E||c component, the peaks are at 3.64 eV, 4.07 eV, 4.57 eV, 5.57 eV, and 7.08 eV, respectively. The obtained peak energy values in the absorption spectra for E||a and E||c are shown in Table II; inside the parentheses, we show the involved Bloch orbitals that contribute to the single-electron transition to that peak value. We found that for the E||a component, all the transitions for five different peak values occur at the Γ point, whereas in E||c, corresponding to the first and the third peak, the transitions are at the T point, while for the rest of the peaks, i.e., the second, fourth, and fifth, the occur at the Γ point. Although, we have not computed the excitonic effects in the absorption spectrum, however, we expect them to be significant, because the exciton

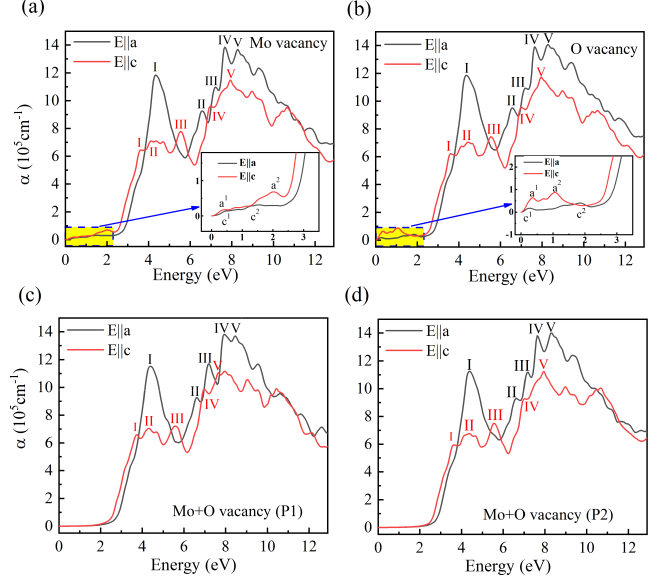


FIG. 14. Absorption spectra of $2 \times 2 \times 1$ supercell of α -MoO₃ for E|| a (red color) and E|| c (black color) with (a) Mo-vacancy, (b) O-vacancy, and (c,d) Mo-O co-vacancies of types P1 and P2, respectively. (black color).

binding energy in MoO₃ has been estimated to be in the range of 21-28 meV [75, 76]. Next, we analyze the optical properties of defective systems of $2 \times 2 \times 1$ supercell of α -MoO₃. Figs. 14(a)- 14(d) show the absorption spectra of the supercell with Mo-vacancy, O-vacancy, and Mo-O co-vacancies of types P1 and P2, respectively. It is obvious from the plots that due to the introduction of vacancies into the system, some new peaks have emerged in the absorption spectra below the main band edge. In the Mo vacancy case (Fig. 14(a)), below the band edge, two peaks are obtained at 0.47 eV (c^1) and 1.23 eV (c^2) for the E||a component, and 0.33 eV (a^1) and 2.0 eV (a^2) in the E||c component (see inset of Fig. 14(a)). In case of the O vacancy (Fig. 14(b)), the peak positions below the band edge are obtained at 0.27 eV (c^1) and 1.86 eV (c^2) for E||a, and 0.36 eV (a^1) and 1.04 eV (a^2) for E||c (see inset of Fig. 14(b)), respectively. Interestingly, there are no peaks obtained below the band edge in the Mo-O co-vacancies of both types. As in the case of the pristine system, for the defective systems also we obtain five different absorption peaks in the absorption spectra corresponding to the Mo, O, and Mo-O co-vacancies (Fig. 14(a)-14(d)). The calculated peak energy values for different defect configurations are presented in Table III.

IV. CONCLUSION

In this work we presented a first-principles DFT-based systematic study of electronic, optical, and magnetic properties of crystalline α -MoO₃ both in its pristine form and with various vacancy configurations. Due to the va-

TABLE II. Calculated peak energy values (eV) from absorption spectra of $2 \times 2 \times 1$ supercell of pristine α -MoO₃. Inside the parentheses, orbitals that contribute to the single electron transition to that obtained peak value are mentioned. v and c indicate the VBM and CBM, and $c+n$ indicates the n th conduction band.

Peak No.	Peak energy values (eV)	
	$E a$	$E c$
I	4.36 ($ v \rightarrow c + 6\rangle$)	3.64 ($ v \rightarrow c + 4\rangle$)
II	6.58 ($ v \rightarrow c + 16\rangle$)	4.07 ($ v \rightarrow c + 4\rangle$)
III	7.15 ($ v \rightarrow c + 20\rangle$)	4.57 ($ v \rightarrow c + 7\rangle$)
IV	7.94 ($ v \rightarrow c + 18\rangle$)	5.57 ($ v \rightarrow c + 12\rangle$)
V	8.44 ($ v \rightarrow c + 22\rangle$)	7.08 ($ v \rightarrow c + 17\rangle$)

TABLE III. Calculated peak energy values (eV) from absorption spectra corresponding to different vacancy configurations of $2 \times 2 \times 1$ supercell of α -MoO₃.

Peak No.	$E a$ (eV)				$E c$ (eV)			
	Mo vacancy	O vacancy	Mo-O co-vacancy (P1)	Mo-O co-vacancy (P2)	Mo vacancy	O vacancy	Mo-O co-vacancy (P1)	Mo-O co-vacancy (P2)
I	4.36	4.37	4.35	4.33	3.63	3.71	3.59	3.62
II	6.58	6.59	6.64	6.57	4.45	4.32	4.35	4.09
III	7.17	7.20	7.19	7.24	5.54	5.59	5.55	5.52
IV	7.63	7.92	7.62	7.67	6.69	6.98	6.97	6.95
V	8.26	8.47	8.28	8.29	7.94	7.64	7.95	7.95

cancies, mid-gap states appear, modifying the properties of the system significantly. From the formation energy calculations, we conclude that O vacancies (in the Mo-rich limit) and Mo-O co-vacancies (in the O-rich limit) are more favorable defects in the α -MoO₃, compared with the Mo vacancies in the system. Although, the pristine α -MoO₃ is a non-magnetic semiconductor, however, our calculations predict that configurations with Mo vacancy and Mo-O co-vacancies give rise to a finite magnetic moment in the system. Mo vacancy leads not only to a very large magnetic moment of $5.98 \mu_B$, but also gives rise to half-metallicity in the system, which can be useful in spintronic applications. In the case of Mo-O co-vacancies, a comparatively lower but still significant magnetic moment of $2.0 \mu_B$ is induced in the system, indicating the possibility of the realization of magnetic behavior in the

material by defect engineering. In the optical absorption spectra of configurations Mo/O vacancies, we observe peaks in the gap region, however, these peaks vanish for configurations with Mo-O co-vacancies just like in the pristine state of α -MoO₃. This suggests that optical absorption spectroscopy can be used for defect identification in the system.

V. ACKNOWLEDGEMENT

P S acknowledges UGC, India, for the senior research fellowship [Grant No. 1330/(CSIR-UGC NET JUNE 2018)]. All the calculation results were obtained using the computational facilities (Spacetime cluster) of the Department of Physics, IIT Bombay.

-
- [1] G. Wei, W. Qin, D. Zhang, G. Wang, R. Kim, K. Zheng, and L. Wang, *Journal of Alloys and Compounds* **481**, 417 (2009).
 - [2] N. A. Chernova, M. Roppolo, A. C. Dillon, and M. S. Whittingham, *Journal of Materials Chemistry* **19**, 2526 (2009).
 - [3] V. S. Saji and C.-W. Lee, *ChemSusChem* **5**, 1146 (2012).
 - [4] S.-H. Lee, Y.-H. Kim, R. Deshpande, P. A. Parilla, E. Whitney, D. T. Gillaspie, K. M. Jones, A. H. Mahan, S. Zhang, and A. C. Dillon, *Advanced Materials* **20**, 3627 (2008).
 - [5] H. You, Y. Dai, Z. Zhang, and D. Ma, *Journal of Applied Physics* **101**, 026105 (2007).
 - [6] J. Meyer, S. Hamwi, M. Kröger, W. Kowalsky, T. Riedl, and A. Kahn, *Advanced materials* **24**, 5408 (2012).
 - [7] Q. Bao, J. Yang, Y. Li, and J. Tang, *Applied physics letters* **97**, 172 (2010).
 - [8] I. A. De Castro, R. S. Datta, J. Z. Ou, A. Castellanos-Gomez, S. Sriram, T. Daeneke, and K. Kalantar-zadeh, *Advanced Materials* **29**, 1701619 (2017).
 - [9] S.-Y. Lin, C.-M. Wang, K.-S. Kao, Y.-C. Chen, and C.-C. Liu, *Journal of sol-gel science and technology* **53**, 51 (2010).
 - [10] D. Xiang, C. Han, J. Zhang, and W. Chen, *Scientific reports* **4**, 1 (2014).
 - [11] S. Balendhran, J. Deng, J. Z. Ou, S. Walia, J. Scott, J. Tang, K. L. Wang, M. R. Field, S. Russo, S. Zhuiykov, *et al.*, *Advanced Materials* **25**, 109 (2013).
 - [12] S. Balendhran, S. Walia, M. Alsaif, E. P. Nguyen, J. Z. Ou, S. Zhuiykov, S. Sriram, M. Bhaskaran, and

- K. Kalantar-Zadeh, *ACS nano* **7**, 9753 (2013).
- [13] F. Ji, X. Ren, X. Zheng, Y. Liu, L. Pang, J. Jiang, and S. F. Liu, *Nanoscale* **8**, 8696 (2016).
- [14] F. Rahman, T. Ahmed, S. Walia, E. Mayes, S. Sriram, M. Bhaskaran, and S. Balendhran, *Nanoscale* **10**, 19711 (2018).
- [15] D. Hanlon, C. Backes, T. M. Higgins, M. Hughes, A. O'Neill, P. King, N. McEvoy, G. S. Duesberg, B. Mendoza Sanchez, H. Pettersson, *et al.*, *Chemistry of Materials* **26**, 1751 (2014).
- [16] B. Gao, H. Fan, and X. Zhang, *Journal of Physics and Chemistry of Solids* **73**, 423 (2012).
- [17] L. Boudaoud, N. Benramdane, R. Desfeux, B. Khelifa, and C. Mathieu, *Catalysis today* **113**, 230 (2006).
- [18] A. Chithambararaj and A. C. Bose, *Journal of Alloys and Compounds* **509**, 8105 (2011).
- [19] H. Sinaim, D. J. Ham, J. S. Lee, A. Phuruangrat, S. Thongtem, and T. Thongtem, *Journal of alloys and compounds* **516**, 172 (2012).
- [20] M. Sreedhara, H. R. Matte, A. Govindaraj, and C. Rao, *Chemistry—An Asian Journal* **8**, 2430 (2013).
- [21] G. R. Patzke, A. Michailovski, F. Krumeich, R. Nesper, J.-D. Grunwaldt, and A. Baiker, *Chemistry of materials* **16**, 1126 (2004).
- [22] Y. Chen, C. Lu, L. Xu, Y. Ma, W. Hou, and J.-J. Zhu, *CrytEngComm* **12**, 3740 (2010).
- [23] B. Hu, L. Mai, W. Chen, and F. Yang, *Acs Nano* **3**, 478 (2009).
- [24] P. Carcia and E. McCarron Iii, *Thin Solid Films* **155**, 53 (1987).
- [25] P.-R. Huang, Y. He, C. Cao, and Z.-H. Lu, *Scientific reports* **4**, 1 (2014).
- [26] F. Li and Z. Chen, *Nanoscale* **5**, 5321 (2013).
- [27] S. O. Akande, A. Chronos, M. Vasilopoulou, S. Kennou, and U. Schwingenschlögl, *Journal of Materials Chemistry C* **4**, 9526 (2016).
- [28] K. Inzani, T. Grande, F. Vullum-Bruer, and S. M. Selbach, *The Journal of Physical Chemistry C* **120**, 8959 (2016).
- [29] T. Das, S. Tosoni, and G. Pacchioni, *Computational Materials Science* **163**, 230 (2019).
- [30] H. Peelaers, M. Chabiny, and C. Van de Walle, *Chemistry of Materials* **29**, 2563 (2017).
- [31] Q. Qu, W.-B. Zhang, K. Huang, and H.-M. Chen, *Computational Materials Science* **130**, 242 (2017).
- [32] S. Bandaru, G. Saranya, N. J. English, C. Yam, and M. Chen, *Scientific reports* **8**, 1 (2018).
- [33] V. Mishra, M. K. Warshi, A. Sati, A. Kumar, V. Mishra, R. Kumar, and P. Sagdeo, *SN Applied Sciences* **1**, 1 (2019).
- [34] V. Mishra, M. K. Warshi, A. Sati, A. Kumar, V. Mishra, A. Sagdeo, R. Kumar, and P. R. Sagdeo, *Materials Science in Semiconductor Processing* **86**, 151 (2018).
- [35] J. Jupille and G. Thornton, *Defects at oxide surfaces*, Vol. 58 (Springer, 2015).
- [36] D. Kan, T. Terashima, R. Kanda, A. Masuno, K. Tanaka, S. Chu, H. Kan, A. Ishizumi, Y. Kanemitsu, Y. Shimakawa, *et al.*, *Nature materials* **4**, 816 (2005).
- [37] Z. Wu, M. Li, J. Howe, H. M. Meyer III, and S. H. Overbury, *Langmuir* **26**, 16595 (2010).
- [38] R. Courths, B. Cord, and H. Saalfeld, *Solid state communications* **70**, 1047 (1989).
- [39] W. Goes, Y. Wimmer, A.-M. El-Sayed, G. Rzepa, M. Jech, A. L. Shluger, and T. Grasser, *Microelectronics Reliability* **87**, 286 (2018).
- [40] P. Deák, M. Lorke, B. Aradi, and T. Frauenheim, *Journal of Applied Physics* **126**, 130901 (2019).
- [41] C. Freysoldt, B. Grabowski, T. Hickel, J. Neugebauer, G. Kresse, A. Janotti, and C. G. Van de Walle, *Reviews of modern physics* **86**, 253 (2014).
- [42] A. Kohan, G. Ceder, D. Morgan, and C. G. Van de Walle, *Physical Review B* **61**, 15019 (2000).
- [43] J. Zheng, G. Ceder, T. Maxisch, W. K. Chim, and W. K. Choi, *Physical Review B* **73**, 104101 (2006).
- [44] M. Venkatesan, C. B. Fitzgerald, and J. M. D. Coey, *Nature* **430**, 630 (2004).
- [45] C. D. Pemmaraju and S. Sanvito, *Physical review letters* **94**, 217205 (2005).
- [46] I. Elfimov, S. Yunoki, and G. Sawatzky, *Physical review letters* **89**, 216403 (2002).
- [47] G. Rahman, V. M. García-Suárez, and S. C. Hong, *Physical Review B* **78**, 184404 (2008).
- [48] G. Rahman, N. U. Din, V. M. Garcia-Suarez, and E. Kan, *Physical Review B* **87**, 205205 (2013).
- [49] M. Khalid, M. Ziese, A. Setzer, P. Esquinazi, M. Lorenz, H. Hochmuth, M. Grundmann, D. Spemann, T. Butz, G. Brauer, *et al.*, *Physical Review B* **80**, 035331 (2009).
- [50] S. Pandey, A. Shukla, and A. Tripathi, *Computational Materials Science* **210**, 111037 (2022).
- [51] Q. Wang, M. Brier, S. Joshi, A. Puntambekar, and V. Chakrapani, *Physical Review B* **94**, 245305 (2016).
- [52] Y. Guo and J. Robertson, *Applied Physics Letters* **105**, 222110 (2014).
- [53] D. Lambert, S. Murphy, A. Lennon, and P. Burr, *RSC advances* **7**, 53810 (2017).
- [54] G. Kresse and J. Furthmüller, *Physical review B* **54**, 11169 (1996).
- [55] G. Kresse and J. Furthmüller, *Computational materials science* **6**, 15 (1996).
- [56] J. J. Mortensen, L. B. Hansen, and K. W. Jacobsen, *Physical Review B* **71**, 035109 (2005).
- [57] G. Kresse and D. Joubert, *Physical review b* **59**, 1758 (1999).
- [58] J. P. Perdew, K. Burke, and M. Ernzerhof, *Physical review letters* **77**, 3865 (1996).
- [59] H. J. Monkhorst and J. D. Pack, *Physical review B* **13**, 5188 (1976).
- [60] H. Ehrenreich and M. H. Cohen, *Physical Review* **115**, 786 (1959).
- [61] P. Ravindran, A. Delin, B. Johansson, O. Eriksson, and J. Wills, *Physical Review B* **59**, 1776 (1999).
- [62] B. S. Dandogbessi and O. Akin-Ojo, *Journal of Applied Physics* **120**, 055105 (2016).
- [63] A. Du, Z. Zhu, and S. C. Smith, *Journal of the American Chemical Society* **132**, 2876 (2010).
- [64] A. Hashimoto, K. Suenaga, A. Gloter, K. Urita, and S. Iijima, *nature* **430**, 870 (2004).
- [65] M. M. Ugeda, I. Brihuega, F. Guinea, and J. M. Gómez-Rodríguez, *Physical Review Letters* **104**, 096804 (2010).
- [66] S. Z. Noby, A. Fakharuddin, S. Schupp, M. Sultan, M. Krumova, M. Drescher, M. Azarkh, K. Boldt, and L. Schmidt-Mende, *Materials Advances* **3**, 3571 (2022).
- [67] S. Chiam, B. Dasgupta, D. Soler, M. Leung, H. Liu, Z. Ooi, L. Wong, C. Jiang, K. Chang, and J. Zhang, *Solar energy materials and solar cells* **99**, 197 (2012).
- [68] J. G. Speight, *Lange's Handbook of Chemistry*, 16th ed.; McGraw-Hill: New York, NY, USA, 1 (2005).

- [69] D. Cao, H. Shu, T. Wu, Z. Jiang, Z. Jiao, M. Cai, and W. Hu, *Applied Surface Science* **361**, 199 (2016).
- [70] A. V. Kuklin, L. V. Begunovich, L. Gao, H. Zhang, and H. Ågren, *Physical Review B* **104**, 134109 (2021).
- [71] A. A. Koós, P. Vancsó, M. Szendrő, G. Dobrik, D. Antognini Silva, Z. I. Popov, P. B. Sorokin, L. Henrard, C. Hwang, L. P. Biró, and L. Tapasztó, *The Journal of Physical Chemistry C* **123**, 24855 (2019).
- [72] M. Itoh, K. Hayakawa, and S. Oishi, *Journal of Physics: Condensed Matter* **13**, 6853 (2001).
- [73] V. Sabhapathi, O. M. Hussain, S. Uthanna, and P. J. Reddy, *Materials Letters* **20**, 175 (1994).
- [74] V. Sabhapathi, O. M. Hussain, S. Uthanna, B. S. Naidu, and P. J. Reddy, *Journal of materials science letters* **14**, 411 (1995).
- [75] M. Shahrokhi, P. Raybaud, and T. Le Bahers, *Journal of Materials Chemistry C* **8**, 9064 (2020).
- [76] W. Fogle and J. H. Perlstein, *Physical Review B* **6**, 1402 (1972).